# Supporting Information

## 5-Acetylsalicylamide as a multifunctional additive for synergistic defect passivation and crystallization control in inverted perovskite solar cells

Ruibo Zhou,[†a] Haoyun Dou,[†a] Tianyi Zhao,[†a] Lei Liu,[a] Zhou Yang,[b] Rongjun Zhao,[*a] Hongqing Ma,[*c] and Hong-En Wang[*a]

[a] College of Physics and Electronic Information, Yunnan Key Laboratory of Optoelectronic Information Technology, Yunnan Normal University, Kunming 650500, China. Email: hongen.wang@ynnu.edu.cn, rjzhao@ynnu.edu.cn

[b] School of Materials Science and Engineering, Shaanxi Normal University, Xi'an 710119, China.

[c] School of Energy & Environmental Science, Yunnan Normal University, Kunming 650500, China. Email: hongqing6010@126.com

[1] These authors contributed equally to this work

## Experimental section

### *1. Materials*

Nickel oxide nanoparticles ($NiO_X$), ITO (transmission greater than 95%) substrates, (2-(3,6-dimethoxy-9Hcarbazol-9-yl)ethyl) Phosphonic acid (MeO-2PACz, 98.0%), and cesium iodide (CsI, 99.99%) were purchased from TCI (Shanghai). 5-Acetylsalicylamide (5-ASA, purity greater than 99.5%), lead iodide ($PbI_2$, 99.99%), formamidinium iodide (FAI), and isopropyl alcohol (IPA, 99.7%) were purchased from Advanced Election Technology Co., Ltd. Dimethyl sulfoxide (DMSO, 99.9%), N,N-dimethylformamide (DMF, 99.9%), and chlorobenzene (CB, 99.8%) were purchased from Sigma Aldrich. Bathocuproine (BCP) and [6,6]phenyl-C61-butyric acid methyl ester (PCBM) were purchased from Xi'an Polymer Light Technology Corp.

### *2. Solution preparation*

The $NiO_X$ nanoparticles were dissolved in deionized water at 20 mg/mL via ultrasonication for 5 min. The MeO-2PACz was dispersed in absolute ethanol at a concentration of 1 mg/mL. For the $FA_{0.95}Cs_{0.05}PbI_3$ perovskite precursor, a 1.4 M solution was prepared by dissolving 228.4 mg FAI, 18.2 mg CsI, 645.4 mg $PbI_2$, and 0.5 mg/mL 5-ASA in a mixture of DMF and DMSO (v/v, 4:1).

*3. Device fabrication and tests*

Patterned ITO substrates were ultrasonically cleaned with detergent, deionized water, acetone, and ethanol for 30 min each, followed by a 15-min ultraviolet-ozone (UVO) treatment. The $NiO_X$ aqueous solution (20 mg $mL^{-1}$) was spin-coated onto the substrates at 4000 rpm for 30 s in ambient air, followed by annealing at 150 °C for 10 min. The resulting $NiO_X$ films were transferred into a nitrogen-filled glovebox. The MeO-2PACz solution (1 mg $mL^{-1}$) was spin-coated onto the $NiO_X$ films at 3000 rpm for 30 s, followed by annealing at 100 °C for 10 min. The perovskite precursor was spin-coated using a two-step process: 2000 rpm for 10 s, followed by 4000 rpm for 40 s. During the second step, 140 μL of CB was dripped onto the film 5 s before the end of the program. The resulting wet films were annealed at 100 °C for 30 min. Subsequently, a PCBM solution in CB (23 mg $mL^{-1}$) was spin-coated at 2500 rpm for 30 s, followed by spin-coating a BCP solution in IPA (0.5 mg $mL^{-1}$) at 5000 rpm for 35 s. Finally, a 120-nm-thick Ag electrode was thermally evaporated onto the BCP layer under a vacuum of $1 \times 10^{-5}$ Pa.

The current density-voltage (*J-V*) characteristics of the devices were measured under simulated AM 1.5G illumination (100 mW/$cm^2$, Oriel Sol3A solar simulator). The light intensity was calibrated using a standard crystalline Si reference cell. The *J-V* curves were acquired with a Keithley 2400 source meter, using a 10-mV voltage step and a 20 ms delay time. The forward scan (0 V to 1.2 V) and the reverse scan (1.2 V to 0 V) were performed under the same measurement conditions.

## *4. Machine Learning*

We used the change in PCE before and after passivation to evaluate passivation performance, with the corresponding output being ΔPCE (ΔPCE = PCE passivated - PCE initial). The input variables were the device's molecular chemistry (e.g., polarity, molecular complexity) and the initial PCE. The ΔPCE dataset was categorized into three classes: ΔPCE<1% (Class-0), ΔPCE:1%-2% (Class-1), and ΔPCE>2% (Class-2). In Class 2, the SHAP values contributed the most to the model's predictions; therefore, the majority of the systems we investigated fall into this category. To handle various data patterns, we employed multiple machine learning models, using 90% of the data for training. A grid search with 10-fold cross-validation was used to train and evaluate five classification models: K-Nearest Neighbors (KNN), Support Vector Machine (SVM), Random Forest (RF), Multi-Layer Perceptron (MLP), and Gradient Boosting (GB). Our analysis indicated that for the single-algorithm scenario, the Random Forest model achieved the highest accuracy, exceeding 80%, and demonstrated strong identification capability for Class-2 passivator molecules.[1]

## *5. DFT calculations*

Electronic structure calculations based on density functional theory (DFT) were performed using the Vienna Ab initio Simulation Package (VASP).[2] [3] The interactions

between ions and electrons were described using the projector augmented wave (PAW) pseudopotentials.[4] [5] The exchange-correlation functional was treated within the Perdew-Burke-Ernzerhof (PBE) generalized gradient approximation (GGA), with dispersion corrections incorporated via the DFT-D3 method.[6] The plane-wave kinetic energy cutoff was set to 400 eV. Brillouin zone sampling utilized a 4×4×1 Monkhorst-Pack k-point grid. Geometric optimizations were performed until the convergence criteria of energy change below $1\times10^{-5}$ eV and atomic forces below 0.05 eV $Å^{-1}$ were satisfied. A 16 Å vacuum space was added to the perovskite slabs. Dipole corrections are applied to the z-direction for all adsorption calculations. All ionic optimizations were done at the gamma point, and the bottom two atom layers were fixed during the optimizations.

*6. Materials characterizations*

The ultraviolet-visible (UV-Vis) absorption spectra were measured using a Shimadzu spectrophotometer. The scanning electron microscopy (SEM) images were taken on a Hitachi Regulus8100. The crystal structures of the samples were analyzed by X-ray diffraction patterns recorded on a Bruker D8 Advance diffractometer with Cu Kα radiation (λ = 1.5418 Å). The steady-state photoluminescence (PL) and time-resolved photoluminescence (TRPL) spectra were acquired using an Edinburgh Instruments setup with a 532 nm excitation laser. Atomic force microscopy (AFM) measurements were performed using a Park Systems CSPM5500. The external

quantum efficiency (*EQE*) was measured using a Newport OPS-A500 system. $^{1}$H nuclear magnetic resonance ($^{1}$H NMR) spectra were recorded on a Bruker AVANCE III HD spectrometer. Equal weights of FAI powder and a mixture of FAI with 5-ASA were dissolved in DMSO-$d_6$. The measurements employed a spectral width of 15 ppm, 64 sampling points, a relaxation delay of 2 seconds, and a 90° pulse angle. Additionally, space-charge-limited current (SCLC) measurements were conducted on hole-only device structures. Key parameters, including carrier mobility and trap-state density, were extracted by applying a bias voltage to generate the space-charge-limited current and analyzing the resultant current-voltage (I-V) characteristics. Mott-Schottky measurements were performed on perovskite solar cells under dark conditions. A small AC perturbation signal (10-50 mV) was applied while scanning the DC bias voltage from negative to positive across the device's operating range. The capacitive response was recorded, and the $1/C^2$-V plot was generated. The flat-band potential was then derived from the linear region of the curve. Electrochemical impedance spectroscopy (EIS) measurements were conducted on perovskite solar cells in the dark. A small AC perturbation signal (10-50 mV) was applied, and the impedance response was measured to obtain the complex impedance spectrum.

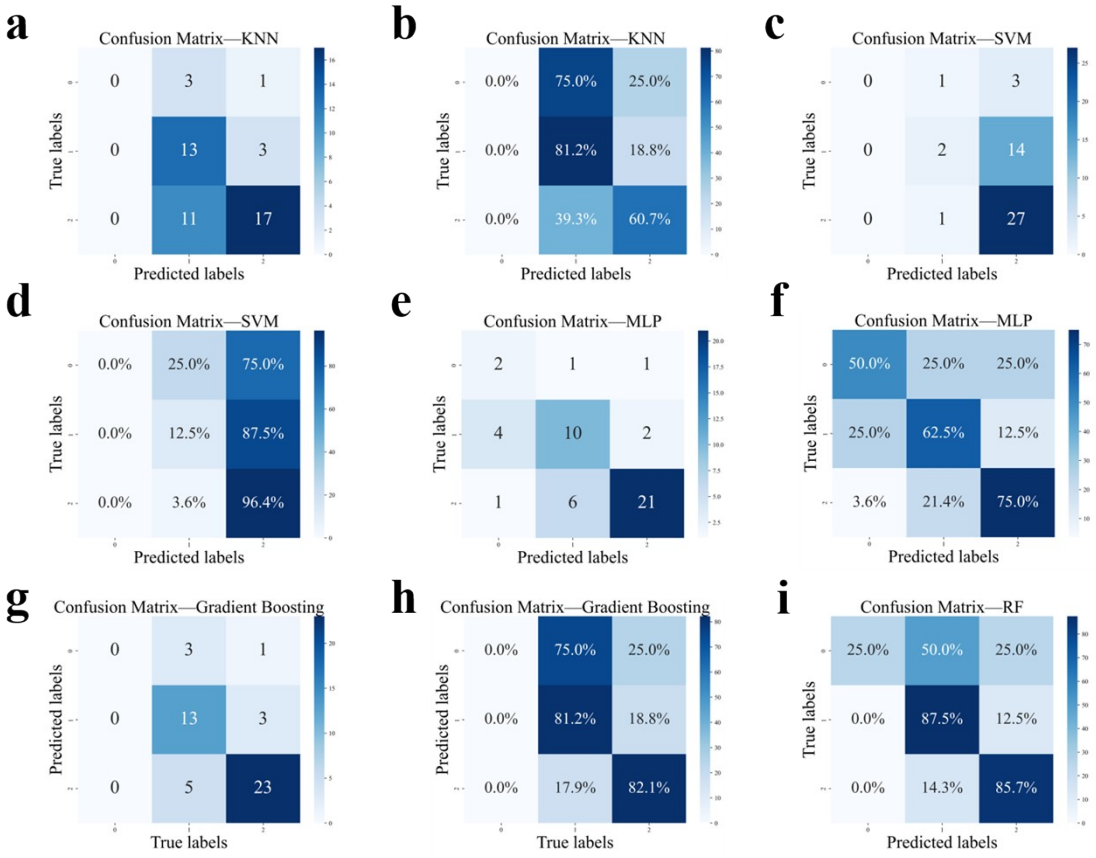


**Fig. S1.** Confusion matrices of five different models on the test set. The KNN model: (a) The horizontal and vertical axes represent the predicted values and true values, respectively; (b) values within the grid indicate model accuracy, with the color bar ranging from 0% to 100%. The SVM model: (c) The horizontal and vertical axes represent the predicted values and true values, respectively; (d) values within the grid indicate model accuracy, with the color bar ranging from 0% to 100%. The MLP model: (e) The horizontal and vertical axes represent the predicted values and true values, respectively; (f) values within the grid indicate model accuracy, with the color bar ranging from 0% to 100%. The GB model: (g) The horizontal and vertical axes represent the predicted values and true values, respectively; (h) values within the grid indicate model accuracy, with the color bar ranging from 0% to 100%. The RF model: (i) values within the grid indicate model accuracy, with the color bar ranging from 0% to 100%.

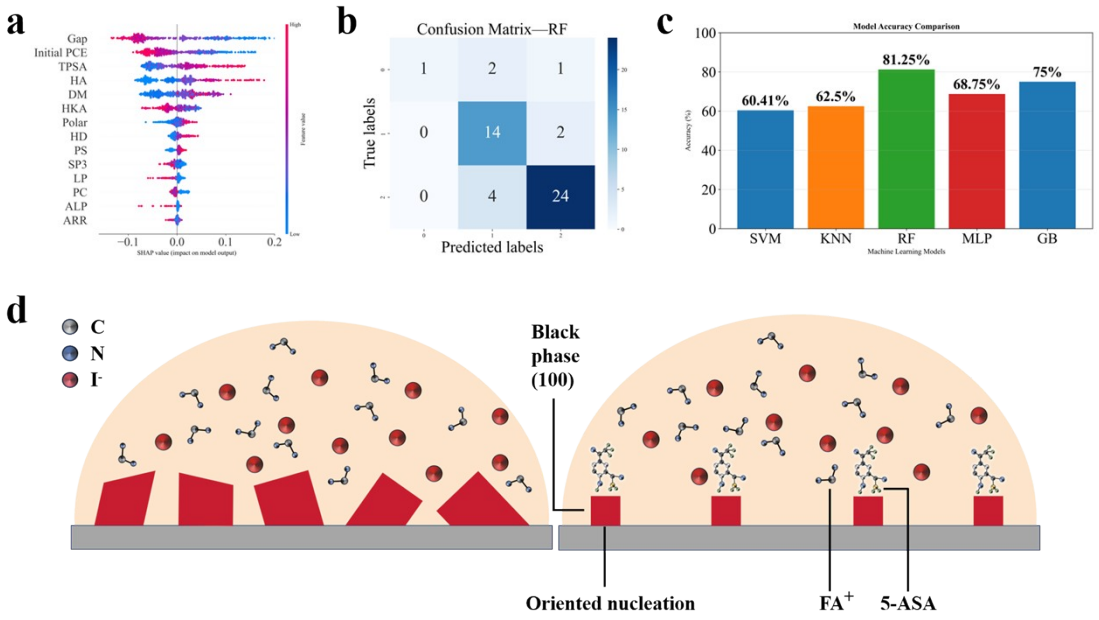


**Fig. S2.** (a) Importance ranking of input features X for Class III in the RF model. The different input features X are arranged in descending order of importance. The color bar, with red and blue indicating high and low values for each feature respectively, illustrates the relationship between the feature values and their corresponding SHAP values in the distribution plot. (b) Confusion matrix of the RF model on the test set. The horizontal and vertical axes represent the predicted values and the true values, respectively. (c) Accuracy calculated by individual ML models. (d) Schematic illustration of the kinetics of the oriented nucleation of perovskite films.

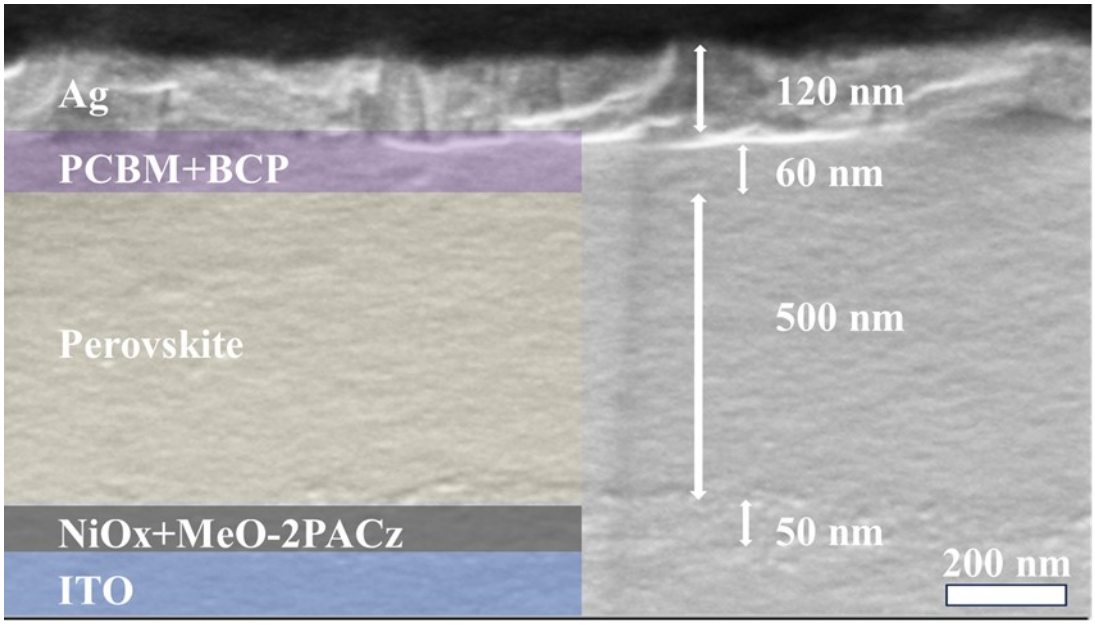


**Fig. S3.** Cross-sectional SEM image of the device.

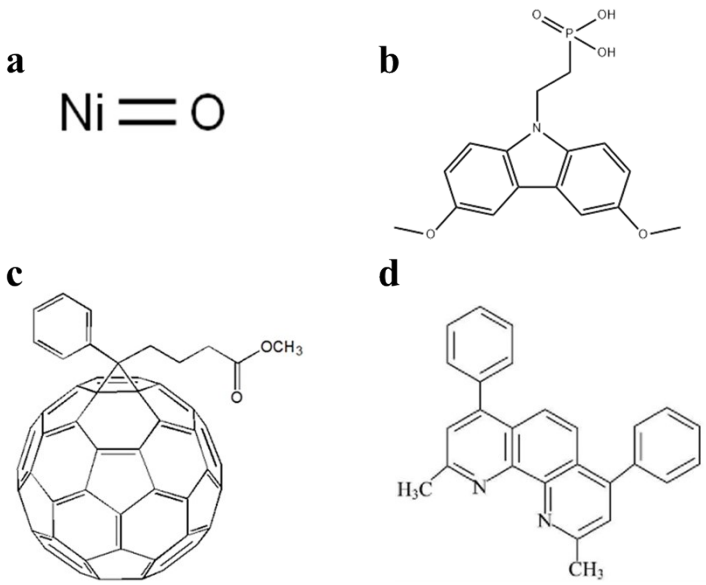


**Fig. S4.** Molecular structure diagram: (a) $NiO_X$, (b) MeO-2PACz, (c) PCBM, (d) BCP.

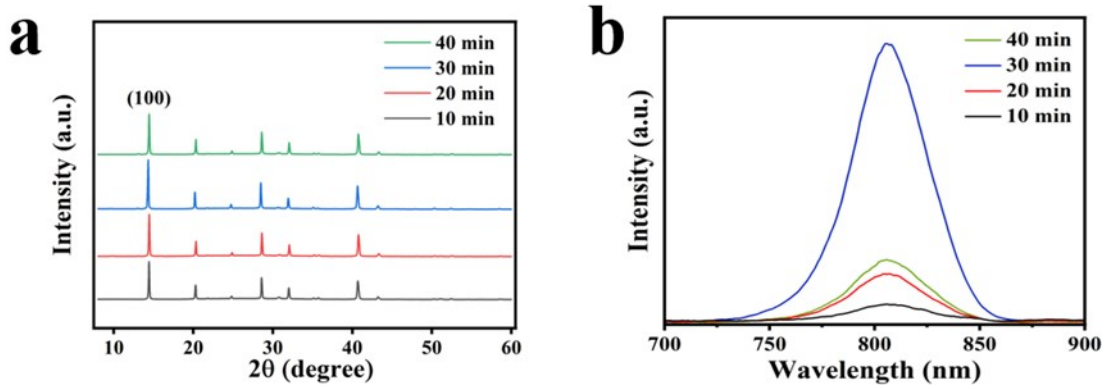


**Fig. S5.** Perovskite thin films under different annealing times: (a) XRD, (b) PL, (c) diagram of differential charge transfer.

**Notes:**

We analyzed the XRD/PL data from films annealed for different times (10-40 min). Crucially, for the 5-ASA-modified films, the (100) diffraction peak intensity

increases more **r**apidly and consistently with annealing time, reaching near-optimal crystallinity faster (e.g., at 30 min) than the control. This suggests that 5-ASA may reduce the activation energy for crystallization or promote more homogeneous nucleation**,** leading to a more efficient and controlled crystallization process.

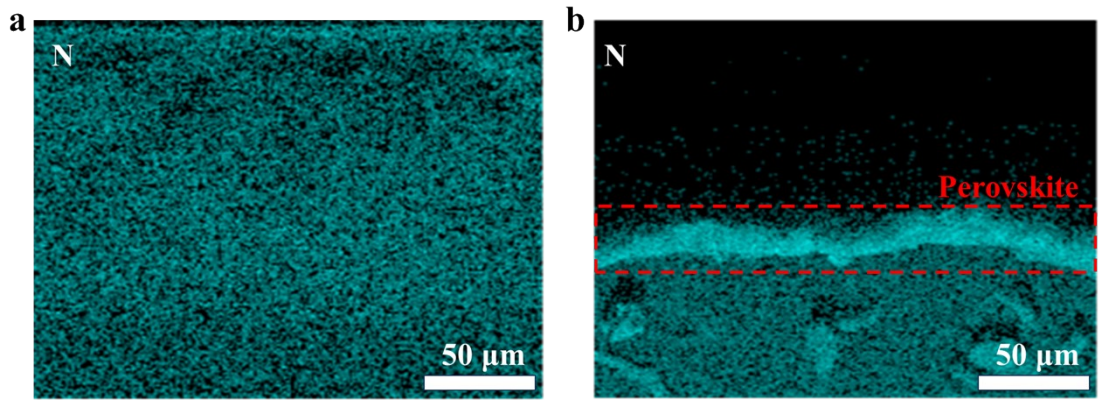


**Fig. S6.** (a) planar and (b) cross-sectional view of SEM-EDX elemental mapping of a 5-ASA-doped $CsPbI_3$ film, evidencing the homogeneous distribution of N signal in the film.

While direct elemental mapping in the (FA,Cs)$PbI_3$ film is complicated by signal overlap, EDX analysis in a model $CsPbI_3$ system shows a homogeneous nitrogen signal from 5-ASA (Fig. S6), consistent with a lack of severe aggregation. This observation provides indirect supports to the conclusion, drawn from the uniform improvements in bulk optoelectronic properties, that 5-ASA is well-dispersed and acts as a bulk passivator.

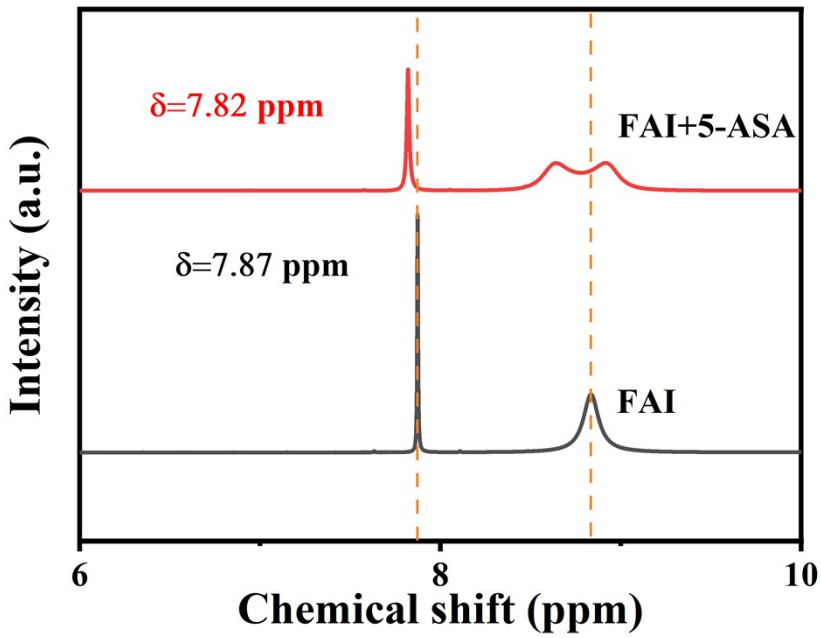


**Fig. S7.** $^{1}$H NMR spectra of FAI and FAI+5-ASA.

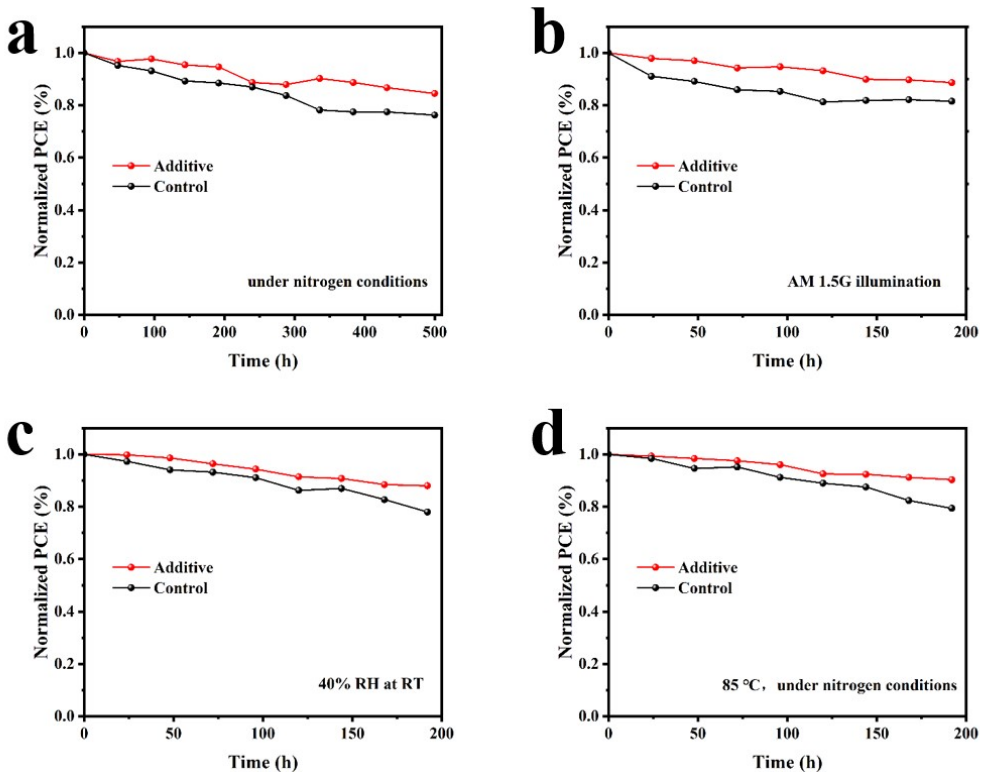


**Fig. S8.** Stability tests of the devices under different conditions: (a) under nitrogen conditions, (b) under continuous illumination, (c) at 40% relative humidity (RH), and (d) at 85 °C in $N_2$.

As shown in Fig. S8a, we evaluated the long-term operational stability of the devices under a nitrogen atmosphere without requiring additional encapsulation. After 500 h, the 5-ASA-modified device retained 85% of its initial power conversion efficiency (PCE). In contrast, the control device maintained only 76% of its initial PCE. The rapid efficiency degradation observed in the control device can be attributed to significant non-radiative recombination at the interfaces between charge carriers, which exacerbates the device performance deterioration. Furthermore, we assessed the stability of the devices under combined stressors, including light exposure, relative humidity (RH), and thermal conditions (85°C in nitrogen), as illustrated in Figs. S8b and 8c. The stability testing results demonstrate that the modified device exhibits superior stability, maintaining robust performance under light, thermal, and humidity challenges.

**Table S1.** Data source, definitions and detailed interpretation of the 26 features.

| Data source | Feature | Detailed interpretation |
|---|---|---|
| DFT calculation | DM (Dipole moment) | The separation of positive and negative charges, indicating the molecule's polarity. |
| | Gap (HOMO-LUMO Gap) | The energy difference between its highest occupied molecular orbital (HOMO) and lowest unoccupied molecular orbital (LUMO). |
| | Poalr (Polarizability) | The ease with which the electron cloud can be distorted under an external electric field. |
| RDkit | ML (Molecular length) | Maximum distance between atoms in the 3D structure of a molecule |
| | LP (Lone pair) | The valence-electron distribution of atoms and their placement in geometrically appropriate positions based on molecular hybridization and VSEPR (Valence Shell Electron Pair Repulsion) theory. |
| | ALP (AliphaticRings) | Rings other than ARR, which are usually non-conjugated rings made of carbon and hydrogen |
| | ARR (AromaticRings) | All the atoms in the ring participate in a ring in a system of conjugated π electrons |
| | SR (SaturatedRings) | Rings in which the carbon-carbon bonds are all single-bonded rings |
| | SP3 (FractionCSP3) | Carbon atoms have other atoms attached to all four of their single bonds |
| | HKA (Hall-Kier alpha) | Based on the electrical properties of atomic charge and chemical |

| | | |
|---|---|---|
| | | bonding, the electron density around each atom on the surface of the molecule. |
| | KAP (Kappa1) | The curvature of space around a single atom or group in a molecule. |
| | CHI (Chi0v) | The average of the electron-absorbing capacity of all atoms in a molecule. |
| | MW (Molecular weight) | Mass of a molecule of a substance, based on 12 as the atomic weight of carbon-12 |
| | HA (Hydrogen bond acceptor count) | Number of atoms or groups in the molecule capable of accepting hydrogen bonds. |
| | HD (Hydrogen bond donor count) | The number of hydrogen atoms in a molecule that can provide hydrogen bonding. |
| | RB (Rotatable bond count) | The number of chemical bonds in a molecule that can rotate freely. |
| Pubchem | EM (Exact Mass) | Calculated by adding the exact masses of the most abundant isotopes of the constituent elements. |
| | MM (Monoisotopic mass) | One of several types of molecular masses used in mass spectrometry. |
| | TPSA (Topological polar surface area) | Total surface area of polar molecules within a compound. |
| | HAC (Heavy atom count) | Number of all atoms in the molecule except hydrogen atoms. |
| | MC (Molecular complexity) | Molecular complexity is calculated by counting the set bits in a molecular fingerprint. |
| | PS (Passivation style) | 1: Bottom surface passivation;<br>2: Bulk passivation;<br>3: top surface passivation. |

| | | |
|---|---|---|
| | PC (Perovskite composition) | 1: $MA^+$-based conventional system;<br>2: Wide-bandgap system;<br>3: $FA^+$-based conventional system. |
| | Initial PCE (PCE of PSCs without treatment) | The un-passivated film quality. |

**Table S2.** Photovoltaic Parameters of PSCs Based on Control and Target Devices.

| Devices | Scan direction | $V_{OC}$ (V) | $J_{SC}$ (mA cm$^{-2}$) | FF (%) | PCE (%) | HI |
|---|---|---|---|---|---|---|
| Control | forward | 1.033 | 25.07 | 71.07 | 18.41 | 0.08 |
| | reverse | 1.067 | 24.80 | 76.21 | 20.17 | |
| Additive | forward | 1.085 | 25.65 | 79.47 | 22.12 | 0.01 |
| | reverse | 1.084 | 25.34 | 79.40 | 21.81 | |

## References


1. J. Liu, H. Lv, P. Wang, G. Hou, Y. Zhao, X. Zhang and Q. Huang, *Journal of Energy Chemistry*, 2026, **112**, 56-63.
2. G. Kresse and J. Furthmüller, *Computational Materials Science*, 1996, **6**, 15-50.
3. J. P. Perdew, K. Burke and M. Ernzerhof, *Physical Review Letters*, 1996, **77**, 3865-3868.
4. P. E. Blöchl, *Physical Review B*, 1994, **50**, 17953-17979.
5. G. Kresse and D. Joubert, *Physical Review B*, 1999, **59**, 1758-1775.
6. S. Grimme, J. Antony, S. Ehrlich and H. Krieg, *The Journal of Chemical Physics*, 2010, **132**, 154104.